# Dynamics of the Emission Spectrum of a Single LH2 Complex: Interplay of Slow and Fast Nuclear Motions

Vladimir I. Novoderezhkin,* Danielis Rutkauskas,† and Rienk van Grondelle†

*A. N. Belozersky Institute of Physico-Chemical Biology, Moscow State University, 119992 Moscow, Russia; and †Department of Biophysics and Physics of Complex Systems, Division of Physics and Astronomy, Faculty of Sciences, Vrije Universiteit, 1081 HV Amsterdam, The Netherlands

ABSTRACT We have studied the relationship between the realizations of static disorder and the emission spectra observed for a single LH2 complex. We show that the experimentally observed spectral fluctuations reflect realizations of the disorder in the B850 ring associated with different degrees of exciton delocalization and different effective coupling of the excitons to phonon modes. The main spectral features cannot be explained using models with correlated disorder associated with elliptical deformations of the ring. A quantitative explanation of the measured single-molecule spectra is obtained using the modified Redfield theory and a model of the B850 ring with uncorrelated disorder of the site energies. The positions and spectral shapes of the main exciton components in this model are determined by the disorder-induced shift of exciton eigenvalues in combination with phonon-induced effects (i.e., reorganization shift and broadening, that increase in proportion to the inverse delocalization length of the exciton state). Being dependent on the realization of the disorder, these factors produce different forms of the emission profile. In addition, the different degree of delocalization and effective couplings to phonons determines a different type of excitation dynamics for each of these realizations. We demonstrate that experimentally observed quasistable conformational states are characterized by excitation energy transfer regimes varying from a coherent wavelike motion of a delocalized exciton (with a 100-fs pass over half of the ring) to a hopping-type motion of the wavepacket (with a 350-fs jump between separated groups of 3–4 molecules) and self-trapped excitations that do not move from their localization site.

## INTRODUCTION

Photosynthesis starts with the absorption of a solar photon by one of the light-harvesting pigment-protein complexes and transferring the excitation energy to the photosynthetic reaction center where a charge separation is initiated (1). These initial and ultrafast events have been extensively investigated in photosynthetic purple bacteria. The bacterial light-harvesting complexes comprise a number of packed pigments circularly arranged in a protein scaffold. The peripheral light-harvesting complex 2 (LH2) from *Rhodopseudomonas* (*Rps.*) *acidophila*, whose crystal structure has been determined with high resolution (2,3), is a highly symmetric ring of nine pigment-protein subunits, each containing two transmembrane polypeptide helixes and three bacteriochlorophyll (BChl) molecules, with the $\alpha$-polypeptide on the inner and the $\beta$-polypeptide on the outer side of the ring. The hydrophobic terminal of the protein binds a ring of 18 tightly coupled BChl molecules with a center-to-center distance of $<1$ nm between neighboring pigments. This ring is responsible for the intense absorption of LH2 peaking at $\sim$850 nm (B850 ring). A second ring of nine weakly interacting BChls is located in the polar region of the protein and is responsible for the absorption at $\sim$800 nm (B800 ring).

From nonlinear spectroscopic studies a consistent physical picture of the excitation dynamics in the B850 ring has emerged (4–6). All basic spectroscopic features can be understood on the basis of a model that includes both the excitonic coupling between pigments and the disorder induced by nuclear motion. Strong excitonic interactions between the chromophores within the B850 ring tend to delocalize the excitation over a number of pigments, whereas the nuclear motions (slow conformational changes of the pigment-protein matrix, fast intrapigment vibrations, and phonon modes) break the symmetry of the complex producing more localized states (7–9). Conventional bulk experiments reveal the details of excitonic relaxation and excitation energy transfer dynamics on a femtosecond/picosecond timescale, but these observations and conclusions are associated with an averaging over a large number of complexes with different realizations of the energetic disorder, which is manifested as inhomogeneous spectral line broadening. On the other hand, although restricted to visualization of dynamics on millisecond/second timescale, single-molecule experiments circumvent this ensemble averaging.

Based on room- and low-temperature single-molecule experiments it has been proposed that the LH2 ring can deviate from the ideally circular structure (10–13). Room-temperature polarized fluorescence (FL) experiments were interpreted in terms of an elliptical absorber and emitter with ellipticity and directions of the principal axis varying as a result of the B800 and/or B850 distortion destroying the rotational symmetry and traveling around the ring on a timescale of seconds (10). The anomalously large splitting of the two major orthogonal excitonic transitions observed in low-temperature polarized FL excitation spectra was attributed to a modulation of the coupling strength in the B850 ring that was asserted to be

*Submitted August 15, 2005, and accepted for publication January 3, 2006.*

Address reprint requests to Danielis Rutkauskas, Fax: 31-20-5987999; E-mail: danielis@nat.vu.nl.



0006-3495/06/04/2890/13 $2.00

doi: 10.1529/biophysj.105.072652

associated with an elliptical deformation (11–13). Spectral fluctuations of different magnitude observed on different timescales were associated with a hierarchical structure of the protein conformational landscape (14). Smaller structural ellipticities were found for loosely packed LH2s in membranes, and were probably partly due to an interplay of the disrupting tip and stabilizing lipid environment (15).

In general, the observed variation of the spectral and functional properties of LH2 suggests that the complex can undergo a variety of deformations or evolve through a number of conformational substates. It is reasonable to assume that such conformational substates or in other words realizations of nuclear coordinates underlie the pattern of the static disorder of pigment site energies and interaction energies between pigments that play a key role in our current understanding of the spectroscopic and energy transfer properties of LH2. In a recent experiment (16,17) we have observed a spectral evolution of LH2 between different conformations at room temperature occurring on a second timescale (corresponding to slow nuclear motions) and manifested by abrupt movements of the fluorescence peak wavelength of individual LH2 complexes between long-lived quasistable levels differing by up to 30 nm. We accounted for these spectral fluctuations on the basis of the modified Redfield theory by modeling the FL profiles for different realizations of the static disorder of the pigment transition energies.

In this article we study in greater detail the mechanism of how different realizations of static disorder are associated with the observed spectral changes of LH2 (16,17). 1), We have found that the experimentally observed spectral fluctuations reflect realizations of the disorder in the B850 ring with different degrees of exciton delocalization and different effective coupling of excitons to phonon modes. 2), The positions and spectral shapes of the main exciton components are determined by the disorder-induced shift of the exciton eigenvalues in combination with a phonon-induced shift and broadening. Being dependent on the realization of the disorder, these factors produce different shapes of the emission profile. 3), In addition, different delocalization and effective coupling to phonons determine a different type of excitation dynamics for each of these realizations. We conclude that experimentally observed quasistable conformational states are characterized by different excitation energy transfer regimes varying from a wavelike motion of a delocalized exciton to a noncoherent hopping of a localized wavepacket and an immobile self-trapped excitation.

## THEORY

We employ the cumulant-expansion method (18) to calculate spectral responses in the presence of strong exciton-phonon coupling. This method allows for an exact solution of spectral line shapes and excitation energy dynamics in a molecule with a single electronic transition (18). In a generalization for molecular aggregates (19) the line shapes are calculated including explicitly a diagonal coupling of nuclear modes to one-exciton states (inducing fluctuations of the energies of excitonic transitions), whereas off-diagonal coupling (inducing relaxation between the exciton eigenstates) is taken into account perturbatively. Linear spectra, i.e., absorption (OD) and nonselective steady-state fluorescence (FL) can be expressed as:

$$OD(\omega) = \omega \sum_{\mathrm{k}} d_{\mathrm{k}}^2 \mathrm{Re} \int_0^\infty dt\, e^{\mathrm{i}(\omega-\omega_{\mathrm{k}})\mathrm{t} - g_{\mathrm{kkkk}}(\mathrm{t}) - \mathrm{R}_{\mathrm{kkkk}}\mathrm{t}};$$

$$FL(\omega) = \omega \sum_{\mathrm{k}} P_{\mathrm{k}} d_{\mathrm{k}}^2 \mathrm{Re} \int_0^\infty dt\, e^{\mathrm{i}(\omega-\omega_{\mathrm{k}})\mathrm{t} + \mathrm{i}2\lambda_{\mathrm{kkkk}}\mathrm{t} - g^{*}_{\mathrm{kkkk}}(\mathrm{t}) - \mathrm{R}_{\mathrm{kkkk}}\mathrm{t}};$$

$$\mathbf{d}_{\mathrm{k}} = \sum_{\mathrm{n}} c_{\mathrm{n}}^{\mathrm{k}} \mathbf{d}_{\mathrm{n}}; \quad R_{\mathrm{kkkk}} = -\sum_{\mathrm{k}' \neq \mathrm{k}} R_{\mathrm{k}'\mathrm{k}'\mathrm{kk}} \tag{1}$$

where $P_{\mathrm{k}}$, $\mathbf{d}_{\mathrm{k}}$, and $\omega_{\mathrm{k}}$ denote the steady-state population, transition dipole moment, and frequency (first moment of the absorption spectrum) of the k-th one-exciton state, $g_{\mathrm{kkkk}}$ is the line-broadening function, $\lambda_{\mathrm{kkkk}}$ is the reorganization energy value for the k-th state. The wavefunction amplitude $c_{\mathrm{n}}^{\mathrm{k}}$ (participation of the n-th site in the k-th exciton state) associates the transition dipole of the exciton state with the molecular transition dipole $\mathbf{d}_{\mathrm{n}}$. It is important to note that our expressions for the linear spectra take into account a relaxation-induced broadening of the exciton states given by their inverse lifetimes, i.e., $R_{\mathrm{kkkk}}$. This term was not present in the original theory of Zhang et al. (19), but applications of the theory demonstrated its importance to fit quantitatively the spectra of molecular assemblies such as J-aggregates (20), the FMO complex (21), the PSII reaction center (22–24), bacterial LH2 antenna (16,17), and the LHCII complex from higher plants (25,26). The inverse lifetime of the k-th state is given by a sum of the relaxation rates within the one-exciton manifold (Eq. 1). The rate of the k' → k population transfer is given by (19):

$$\begin{aligned} R_{\mathrm{kkk'k'}} = -2\mathrm{Re} \int_0^\infty dt\, \hat{W}(\omega_{\mathrm{kk'}}, t) \{ \ddot{g}_{\mathrm{kk'k'k}}(t) \\ - \{ \dot{g}_{\mathrm{k'kk'k'}}(t) - \dot{g}_{\mathrm{k'kkk}}(t) + 2i\lambda_{\mathrm{k'kk'k'}} \} \times \{ \dot{g}_{\mathrm{k'k'kk'}}(t) \\ - \dot{g}_{\mathrm{kkkk'}}(t) + 2i\lambda_{\mathrm{k'k'kk'}} \} \} \\ \hat{W}(\omega_{\mathrm{kk'}}, t) = \exp\{ -i\omega_{\mathrm{kk'}} t - g_{\mathrm{kkkk}}(t) \\ - g_{\mathrm{k'k'k'k'}}(t) + 2g_{\mathrm{k'k'kk}}(t) + 2i(\lambda_{\mathrm{k'k'kk}} - \lambda_{\mathrm{k'k'k'k'}})t \}, \end{aligned} \tag{2}$$

where $\omega_{\mathrm{kk'}} = \omega_{\mathrm{k}} - \omega_{\mathrm{k'}}$. The relaxation tensor in the form of Eq. 2 is denoted as the modified Redfield tensor (27) to distinguish it from the standard Redfield tensor obtained in the limit of weak exciton-phonon coupling. The g-functions and λ-values in Eqs. 1 and 2 are:

$$\begin{aligned} g_{\mathrm{kk'k''k'''}}(t) = -\int_{-\infty}^{\infty} \frac{d\omega}{2\pi\omega^2} C_{\mathrm{kk'k''k'''}}(\omega) \left[ \coth \frac{\omega}{2k_{\mathrm{B}}\mathrm{T}} (\cos\omega t - 1) \right. \\ \left. - i(\sin\omega t - \omega t) \right] \\ \lambda_{\mathrm{kk'k''k'''}} = -\lim_{\mathrm{t}\to\infty} \frac{d}{dt} \mathrm{Im}\{ g_{\mathrm{kk'k''k'''}}(t) \} = \int_{-\infty}^{\infty} \frac{d\omega}{2\pi\omega} C_{\mathrm{kk'k''k'''}}(\omega), \end{aligned} \tag{3}$$

where $C_{\mathrm{kk'k''k'''}}(\omega)$ is the matrix of the spectral densities in the eigenstate (exciton) representation, which reflects coupling of one-exciton states to a manifold of nuclear modes (see next section). In principle, coupling to nuclear motions with arbitrary timescales can be included explicitly in the g-function. But it is convenient to consider separately the action of fast and slow nuclear motions.

### Fast modes

Electronic transitions in a pigment molecule (or collective excitonic transitions in a cluster of strongly coupled pigment molecules) are affected

by fast intra- and intermolecular vibrations, phonon modes of the protein environment, etc., that is all these factors cause the so-called dynamic disorder. In the frequency range of 10–2000 $cm^{-1}$ (as revealed by fluorescence line-narrowing (28), hole-burning (29), and molecular dynamic simulations (30)) these modes determine the homogeneous line broadening (represented by $g_{kkkk}$) of the exciton transitions, a red shift of the zero-phonon lines (ZPL) (which is equal to the reorganization energy value $\lambda_{kkkk}$), and the Stokes shift of the emission maximum of the k-th exciton state (equal to $2\lambda_{kkkk}$). Equation 3 relates these quantities to the spectral density in the eigenstate basis $C_{kkkk}(\omega)$. The latter (as well as the $C_{kk'k''k'''}(\omega)$ quantities needed to calculate the relaxation tensor) can be obtained from the matrix of the spectral densities in the site representation $C_{nmn'm'}(\omega)$.

To simplify the matter we assume only a diagonal electron-phonon coupling in the site representation, i.e., nuclear modes induce fluctuations of the pigment site energies without acting on the intermolecular couplings. Generally, there may be some correlations between fluctuations acting on different sites, but we restrict to the simplest case of uncorrelated dynamic disorder. This model implies that each molecule has its own independent thermal bath. We further suppose that the spectral density function of each such bath is site independent, i.e., spectral density in the site representation is $C_{nmn'm'}(\omega) = \delta_{nm}\delta_{nn'}\delta_{mm'}C(\omega)$. Transformation to the eigenstate representation yields:

$$C_{kk'k''k'''}(\omega) = \sum_n c_n^k c_n^{k'} c_n^{k''} c_n^{k'''} C(\omega). \quad (4)$$

Equation 4 shows that diagonal phonon coupling in the site representation results in both diagonal and off-diagonal couplings in the exciton basis. To construct the spectral density profile we use the sum of an overdamped Brownian oscillator and resonance contributions due to high-frequency modes:

$$C(\omega) = 2\lambda_0 \frac{\omega\gamma_0}{\omega^2+\gamma_0^2} + \sum_{j=1,2\ldots} 2\lambda_j\omega_j^2 \frac{\omega\gamma_j}{(\omega_j^2-\omega^2)^2+\omega^2\gamma_j^2},$$
$$\lambda_j = S_j\omega_j,\ \lambda = \int_{-\infty}^{\infty}\frac{d\omega}{2\pi\omega}C(\omega) = \lambda_0 + \sum_{j=1,2..}\lambda_j, \quad (5)$$

where $\lambda$ is the reorganization energy in the site representation, $S_j$ is the Huang-Rhys factor of the j-th vibrational mode in the site representation. Parameters of the temperature-independent spectral density (frequencies $\omega_j$, couplings $\lambda_j$, and damping constants $\gamma_j$ for high-frequency vibrations together with the coupling $\lambda_0$, and damping $\gamma_0$ for Brownian oscillator) are obtained from the fluorescence line-narrowing spectra (FLN), and further adjusted from the simultaneous fit of OD/FL spectra at different temperatures.

Note that according to Eqs. 3–5 the line-broadening functions and reorganization energies of the k-th exciton state in the eigenstate representation ($g_{kkkk}$ and $\lambda_{kkkk}$) are smaller than in the site representation by a factor of $1/\sum(c_n^k)^4$ (this factor connects $C_{kkkk}(\omega)$ and $C(\omega)$ in Eq. 4). The latter quantity is known as the inverse participation ratio (*PR*) and is equal to the delocalization length of individual exciton state (31–33). In the literature there exist many other definitions of delocalization length reflecting different aspects of the exciton dynamics, and therefore yielding different ''exciton sizes'' for the same system. The relation between them has been studied in great detail (7–9).

## Slow modes

Slow nuclear motions associated with conformational changes of the pigment protein in a native membrane or when immobilized in a gel, on a mica surface, etc., and occurring on the microsecond to second timescale, result in the so-called static disorder of the pigment electronic transition energies (i.e., the nonequivalence of pigment site energies—transition energy of each pigment in the complex deviates from some average value by an amount specific to that pigment) manifested as inhomogeneous broadening in conventional bulk spectroscopic experiments or the time dependence of fluorescence spectral parameter traces in single-molecule measurements (16,17).

We model different realizations of the static disorder (combinations of pigment site energy deviations from the nondisordered value), corresponding to different complexes measured simultaneously in the bulk, or one complex at different moments in time in single-molecule experiments, by random uncorrelated shifts of the site energies (diagonal disorder). Numerical diagonalization of the one-exciton Hamiltonian yields eigenstate energies $\omega_k$ and eigenfunctions $c_n^k$, required to calculate OD/FL spectra for one realization of the static disorder. Such calculations with a number of realizations of static disorder allows for a statistical characterization and comparison of the resulting spectra with the results of single-molecule experiment or with the bulk spectra after averaging of spectra calculated for different realizations of the disorder.

## Combined action of slow and fast modes

Notice that in the absence of exciton-phonon coupling the $\omega_k$ value corresponds to ZPL position of the k-th exciton level. In the weak coupling limit ZPLs are slightly broadened due to bath-induced exciton relaxation but the $\omega_k$-value still corresponds to the ZPL position and coincides with the maximum of the absorption and emission of the k-th state.

In the case of strong coupling with phonons (Eq. 1) the ZPL position is $\omega_k - \lambda_{kkkk}$, i.e., red-shifted with respect to the eigenvalues of a free-exciton Hamiltonian $\omega_k$. The first moment of the OD is at $\omega_k$, whereas the first moment of FL is $\omega_k - 2\lambda_{kkkk}$. Static disorder induces random shifts of the eigenvalues $\omega_k$. In their turn, the line-broadening function $g_{kkkk}$ (i.e., phonon-induced broadening) and reorganization energy $\lambda_{kkkk}$ (together with the Stokes shift of the k-th level, i.e., $2\lambda_{kkkk}$) are also affected by the static disorder being proportional (see Eqs. 3 and 4) to a disorder-dependent participation ratio $PR_k = \sum_n(c_n^k)^4$ ($PR_k$ value is dependent on the specific realization of the static disorder through the wavefunction amplitudes $c_n^k$). It has been well established (31–33) that an increase in static disorder (given by the full width at half-maximum (FWHM) of the Gaussian distribution from which the pigment site energy shifts are drawn) on the average increases the $PR_k$ values for different realizations of the static disorder, thus increasing the effective dynamic disorder value, i.e., the phonon induced broadening of the exciton states and reorganization shift. Furthermore, an increase in static disorder induces a larger spread of the $PR_k$ values corresponding to different realizations, thus increasing the spread of the line broadenings and reorganization shifts.

Thus, both the positions of the exciton levels (given by $\omega_k - \lambda_{kkkk}$) and the linewidths (determined by $g_{kkkk}$) depend on a combined action of static and dynamic disorder. In particular, the experimentally measured distribution of the ZPL positions (as obtained from a hole-burning experiment for $k = 0$, or studied by a single-molecule technique) includes the disorder of the purely exciton eigenvalues $\omega_k$, in combination with the variation of reorganization-induced shifts $\lambda_{kkkk}$. The amount of this additional reorganization-induced disorder increases in proportion to the exciton-phonon coupling strength $\lambda_j$ and the amount of static disorder that makes the reorganization effects more pronounced in a more disordered system with larger site inhomogeneity.

In the case of the LH1 antenna or the B850 ring from LH2 the static disorder has its most prominent effect on the lowest exciton states, especially $k = 0$ ((8,33,34), and examples given below). Realizations of strong disorder produce more localized and more red-shifted states. The reorganization energy for these realizations is also larger, inducing a further red shift. Moreover, these red-shifted states feature a more pronounced phonon/vibrational wing (because the line-broadening function $g_{kkkk}$ increases for localized states with bigger $PR_k$ value). Thus, the character of the slow conformational changes of the complex significantly influences the effective coupling of the exciton states with the fast nuclear motions (given by Eq. 4), producing different phonon-induced broadening and reorganization energy effects. Thus one can expect a red shift and broadening of the FL spectrum for conformations of the complex with broken symmetry that are associated with a large disorder of the site energies.

Complexes in a more symmetric configuration are expected to conform with the classical excitonic picture (no static disorder). The corresponding

spectral profiles are not shifted and as will be shown later are broadened predominantly due to exciton relaxation.

These described spectral trends were observed in our study of fluorescence fluctuations of single LH2 (16,17). Single complex fluorescence spectra exhibited large red and blue shifts occurring on a second timescale that were accompanied by spectral broadening. These observations are interpreted on the basis of the proposed model.

## Model of LH2 antenna

The LH2 spectral lineshapes and their dynamics are determined by the coupling of electronic excitations to a manifold of nuclear modes (both fast and slow). Fast nuclear modes define the optical line shapes both in conventional (18) and in single-molecule spectroscopy (35). Slow nuclear motions associated with conformational changes of the pigment protein on a microsecond to second timescale are responsible for the change of realizations of static disorder. It is reasonable to suppose that the experimentally observed quasistable states of single LH2 fluorescence spectral traces, characterized by different line shape and peak position, can be treated as different equilibrium positions of the nuclear coordinates, i.e., different realizations of the static disorder (36,37). We hypothesize that transitions between these states occur due to thermal nuclear motion. We do not consider here the dynamics of such transitions but rather restrict ourselves to a modeling of fluorescence line shapes for different realizations of the static disorder. Our model takes into account excitonic interactions within the B850 ring, the presence of static disorder of pigment site energies, and strong coupling of electronic excitations to phonons.

To construct a one-exciton Hamiltonian, the unperturbed transition energies of BChl 850($\alpha$) and BChl 850($\beta$) were taken as 12,275 and 12,125 $cm^{-1}$, respectively. The energies of the $1\alpha1\beta$, $1\beta2\alpha$, $1\alpha2\alpha$, $1\beta2\beta$, and $1\alpha2\beta$ pigment-pigment interactions were taken to be 291, 273, −50, −36, and 12 $cm^{-1}$, respectively, according to Sauer et al. (38). The static disorder was described by uncorrelated perturbations of the transition energies randomly chosen from a Gaussian distribution with the FWHM of $\sigma$. Numerical diagonalization of the Hamiltonian (for each realization of the disorder) gives the energies of the exciton states $\omega_k$ and the wavefunction amplitudes $c_n^k$ (participation of the n-th site in the k-th exciton state).

The absorption and fluorescence line shapes are calculated using Eqs. 1–5. To reproduce the peak positions and the low-frequency wings of the OD/FL spectra, it is not necessary to include the high-frequency part of the spectral density function (second term in Eq. 5). Thus, we assume that the spectral density function $C(\omega)$ has the form of a single overdamped Brownian oscillator with coupling parameter $\lambda = \lambda_0$ and relaxation time $\tau = 1/\gamma_0$ (keeping just the first term in Eq. 5). In our model $\lambda$ and $\tau$ (as well as $\sigma$) are site-independent parameters adjusted from the fit of the bulk OD and FL spectra. All experimental data presented below were acquired at room temperature and the simulation of the data was performed with the corresponding parameters.

## RESULTS AND DISCUSSION

The experiment we will describe by our modeling consists of collecting series of FL spectra of single LH2 complexes of *Rhodopseudomonas acidophila* at room temperature (16,17). In this experiment complexes were immobilized by the electrostatic interaction with a glass coverslip treated with the poly-l-lysine, and submerged in an oxygen-free buffer containing detergent. Complexes were excited with linearly polarized laser light at 800 nm spectrum of LH2. The polarization sensitivity of the detection was found to be insignificant and thus no correction was required.

Fig. 1 presents an average of single-molecule FL spectra in time and over particles as well as the distribution of the FL peak positions together with corresponding results of the modeling. The averaged FL profile has a maximum near 870 nm. Realizations with the FL peak near this wavelength occur with the highest probability. The data are reproduced with parameters $\sigma = 370\ cm^{-1}$, $\lambda = 390\ cm^{-1}$, and $\tau = 50$ fs. Notice that the OD spectrum of the B850 ring of LH2 complex in vivo can be reproduced with the same $\sigma$ and $\tau$, and $\lambda = 220\ cm^{-1}$ (data not shown). Most probably, this difference in $\lambda$ reflects the different strength of exciton-phonon coupling for immobilized and in vivo complexes.

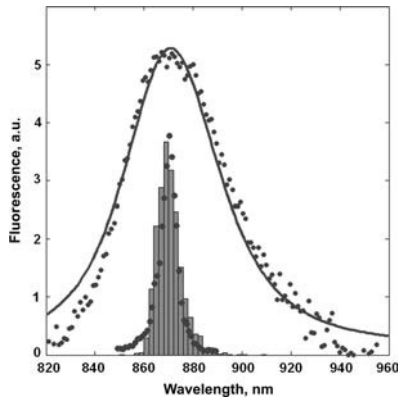


FIGURE 1 Experimental FL profile averaged in time and over particles (*points*) and calculated FL spectrum averaged over realizations of the static disorder (*solid line*). The histogram shows the distribution of peak positions of the experimental FL spectra (*points*) and the same distribution for the calculated FL spectra (*bars*).

Fig. 2 shows averages of experimental and calculated FL profile occurrences with the peak positions within 859–861 nm, 869–871 nm, and 889–891 nm. Red-shifted single-molecule profiles on the average are significantly broadened and display a specific shape with a broader short-wavelength wing. Spectra with intermediate and blue-shifted peak position feature regular FL asymmetry, i.e., a broader long-wavelength tail. Notice that the blue-shifted spectra are also broader than those with intermediate peak position. All these spectral features are satisfactorily reproduced by our model.

Our modeling of the spectra shows that the line shapes associated with the various peak positions are determined by a specific exciton structure corresponding to specific realizations of static disorder. Fig. 2 shows contributions of three lowest exciton components ($k = 0$, $k = -1$, and $k = 1$) to the red-shifted, intermediate, and blue-shifted FL profiles (these components are averaged over realizations that result in the corresponding peak position). The contributions from the higher exciton states ($k = -2$, $k = 2$, ...) can be neglected due to their small dipole strength and insignificant population (but they are still included in the calculation of the whole FL profiles). The three types of exciton structure shown in Fig. 2 correspond to different degrees of delocalization of exciton states. To study this relationship in more detail we have calculated the $PR_k$ values for all the realizations of

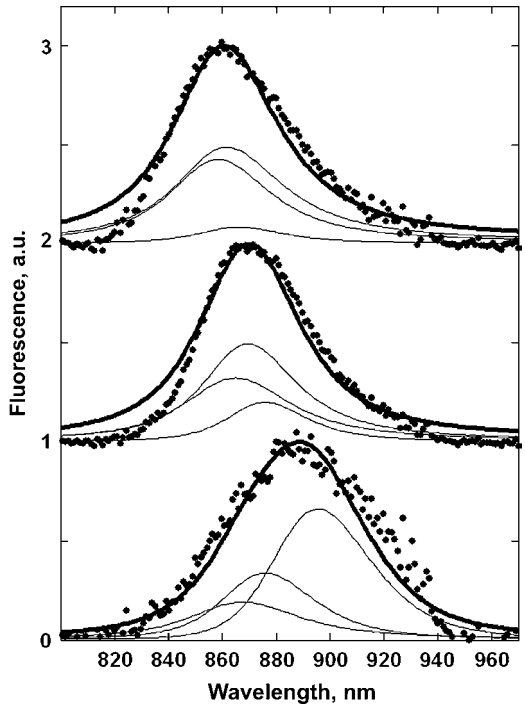


FIGURE 2 Experimental (*points*) and calculated (*solid lines*) FL profiles averaged over realizations with peak positions in the ranges 859–861 nm (*top*), 869–871 nm (*middle*), and 889–891 nm (*bottom*). The calculated emission spectra are shown together with the contributions from the three lowest exciton components (*thin solid lines*). Both measured and calculated spectra are normalized to unity. The value of uncorrelated diagonal disorder is 370 $cm^{-1}$.

static disorder (Fig. 3) and separated them into groups corresponding to blue-shifted, intermediate, and red-shifted spectral profile peak positions (Fig. 4).

Delocalization of the exciton states contributing to the steady-state FL can be characterized by the thermally averaged participation ratio, $\langle PR \rangle$, defined as an average of $PR_k$ values of the individual exciton states weighted with the steady-state populations of those states. $\langle PR \rangle$ values corresponding to the blue, intermediate, and red-shifted FL positions shown in Fig. 2 are 0.098, 0.118, and 0.245, respectively, reflecting the increasingly localized character of the exciton states contributing to the redder FL spectrum.

## Participation ratio for different realizations of static disorder

Fig. 3 shows the $PR_k = \sum_n (c_n^k)^4$ values for the five lowest exciton levels (i.e., $k = 0, -1, 1, -2$, and 2) of LH2 calculated for 2000 realizations of the disorder. Each point corresponds to the $PR_k$ value of one exciton state for one realization of the static disorder as a function of the wavelength of the ZPL of this state (the position of ZPL is $\omega_k - \lambda_{kkkk}$ on the energy scale). Averaging of the *PR* values corresponding to exciton states with ZPLs within narrow

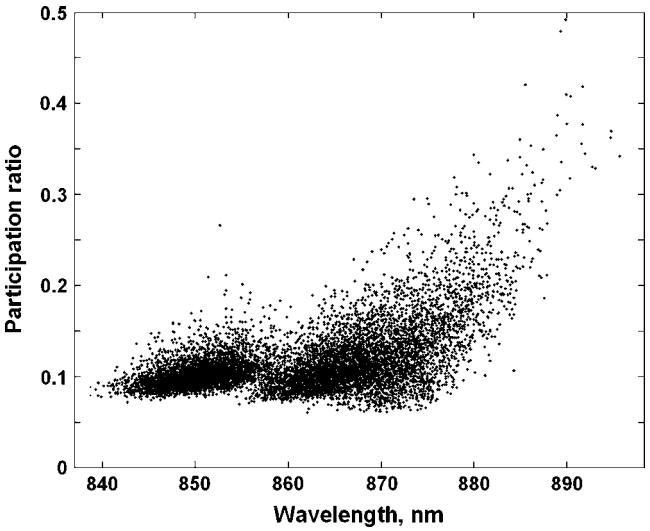


FIGURE 3 The $PR_k$ values for the five lowest exciton levels (i.e., $k = 0, -1, 1, -2$, and 2) calculated for 2000 realizations of the disorder. Each point shows the *PR* value for a certain one-exciton state as a function of the wavelength of the ZPL of this state.

wavelength intervals results in a smooth *PR* curve well known for LH2/LH1 complexes, i.e., almost constant in the middle of the long-wavelength absorption band with an increase on the red side (8,33,34,39). Fig. 4 shows the distributions of $PR_k$ values for each of the exciton states taken from the 2000 realizations shown in Fig. 3 corresponding to spectral profiles with peak positions in the ranges 858–862 nm, 869–871 nm, and 887–894 nm. Note that this is a statistical representation of data similar to Fig. 2 although the intervals of blue- and red-shifted spectral profile maxima are wider to collect more occurrences.

The *PR* values of the exciton states corresponding to blue-shifted FL spectra are 0.085–0.13 for the higher states ($k = \pm 1, \pm 2$) and 0.065–0.12 for the lowest one ($k = 0$) (Fig. 4). These values are close to the homogeneous limit. That is, for a circular aggregate of $N$ molecules $PR = 1/N$ for the lowest and $3/2N$ for the higher states in the absence of the static disorder. For LH2 with $N = 18$ this results in 0.056, and 0.083, respectively. So, we conclude that the exciton states that result from realizations of static disorder corresponding to blue-shifted spectra are not significantly destroyed by the disorder. As a result in this case the exciton structure is also not too different from that of the homogeneous ring, i.e., most of the dipole strength is concentrated in two degenerate levels ($k = \pm 1$), whereas the lowest state ($k = 0$) is almost forbidden due to the symmetry of the ring. The room-temperature emission originates mostly from the degenerate $k = \pm 1$ pair giving rise to a blue-shifted FL (Fig. 2, *top frame*).

FL profiles with an intermediate peak position result from realizations of stronger static disorder (Fig. 4, *middle frame*). This situation corresponds to an increase in the splitting between the exciton levels and a more localized character of

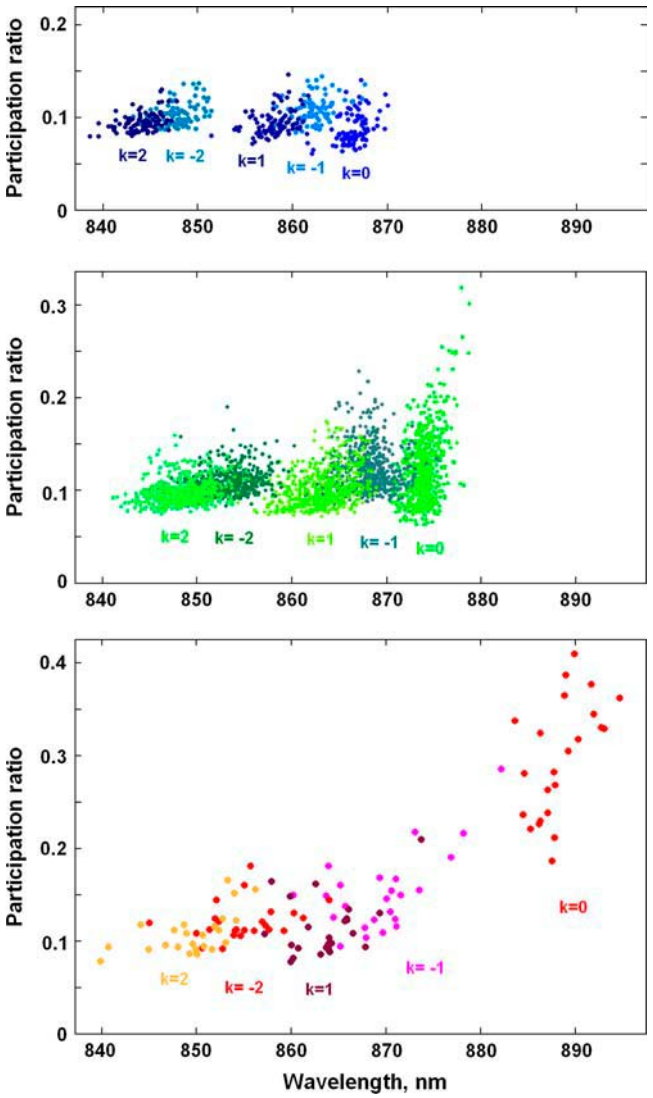


FIGURE 4 The *PR* values for realizations with the fluorescence peaks within 858–862 nm (*top*), 869–871 nm (*middle*), and 887–894 nm (*bottom*) taken from realizations shown in Fig. 3. For each group of realizations the *PR* values for the five lowest exciton levels are marked by different colors. The position of each point on the wavelength axis is given by the ZPL of the corresponding exciton state.

the exciton states yielding $PR_k$ values that have increased up to 0.15–0.20 for the $k = \pm 1$ and up to 0.30 for the lowest $k = 0$ state. This red-shifted and more localized $k = 0$ state also becomes more radiant borrowing some of the dipole strength from higher levels so its contribution to the FL profile becomes more significant (Fig. 2, *middle frame*).

The bottom frame of Fig. 4 illustrates $PR_k$ values of exciton states corresponding to red-shifted FL profiles. In this case the exciton structure is very strongly perturbed by the disorder, which induces a large splitting between the energy levels, in particular, the splitting between the $k = \pm 1$ and the lowest $k = 0$ state is increased significantly (as compared with the blue-shifted and intermediate spectral profiles). Due to this large splitting between excitonic energy levels FL mostly originates from the lowest state, which is now strongly allowed and red-shifted. Its localized character ($PR = 0.2$–$0.4$) gives rise to an increased strength of the effective exciton-phonon coupling (proportional to the $PR_k$ value). Such an increased coupling results in the broadening of the FL profile together with an additional red shift (Fig. 2, *bottom frame*).

## Relaxation-induced broadening

We have seen that an increase in the red shift (because of the low exciton eigenvalue and reorganization shift) is accompanied by enhanced exciton-phonon coupling in the exciton representation (Eq. 4), which produces an increasingly larger broadening of the FL spectra. Another line-broadening factor that determines the width of the blue-shifted FL spectra is exciton relaxation. Typically due to predominant downhill relaxation the inverse lifetime increases for the higher levels. In our model $R_k = 16$, 29, 44, and 57 $ps^{-1}$ for the $k = 0$, $-1$, 1, and $-2$ levels, respectively. The more pronounced relaxation broadening of the $k = \pm 1$ levels results in a larger width of the blue-shifted FL spectra (determined mostly by the $k = \pm 1$ emission). Notice that in the absence of relaxation a blue shift would be always accompanied by a narrowing of the FL line because the $k = \pm 1$ levels are always narrower than the lowest one (for a disordered complex) due to their smaller *PR* values and, as a result, a smaller value of the line-broadening function. Disregarding exciton relaxation it would be impossible to explain the observed broadening of the blue-shifted FL spectra (Fig. 5).

Thus, we conclude that the blue-shifted FL lineshape is determined by delocalized exciton states broadened due to fast exciton relaxation, whereas the broadening of the red-shifted FL profiles originates from a localized excitation dressed by phonons. Switching between these two limits is driven by slow nuclear motions.

## Exciton wavefunctions in the site representation

Analysis of the $PR_k$ values suggests a different degree of delocalization for each of the three spectral profiles shown in Fig. 2. This can also be illustrated by a straightforward visualization of the corresponding exciton wavefunctions. As an example we selected one typical realization of the static disorder with a blue-shifted FL peak position at 858 nm, an intermediate one at 871 nm, and two red-shifted ones at 894 nm. The corresponding thermally averaged $\langle PR \rangle$ values are 0.087, 0.14, 0.25, and 0.35, corresponding to a delocalization over 11, 7, 4, and 3 pigment molecules, respectively. Fig. 6 (*left frames*) shows the shifts of the transition energies of the sites from $n = 1$ to $n = 18$ for these realizations. For the same realizations we show the squared wavefunction amplitudes $(c_n^k)^2$ for $k = 0$, i.e., the participation of the n-th site in the lowest $k = 0$ exciton state (Fig. 6,

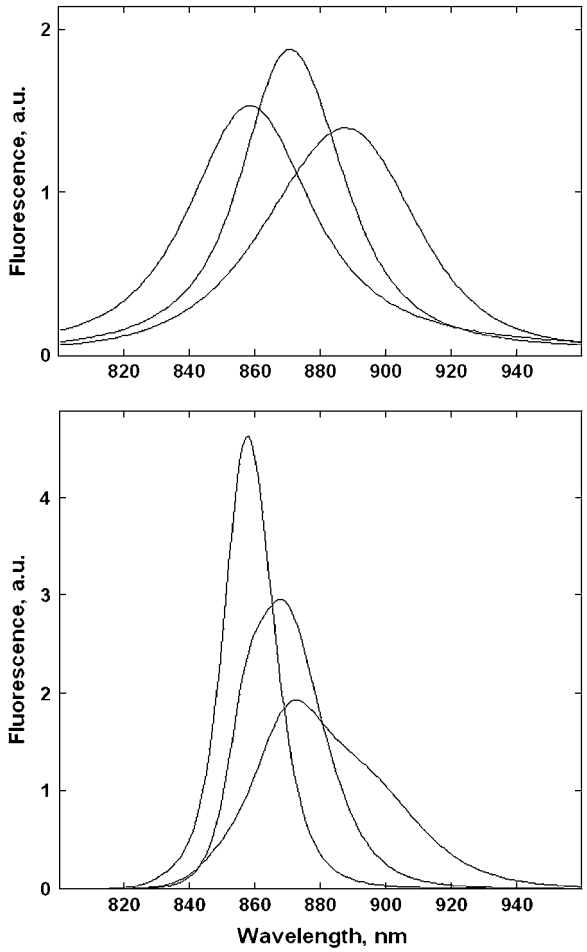


FIGURE 5 (*Top frame*) Calculated FL profiles averaged over realizations peaking near 860, 870, and 890 nm. The spectra are not normalized and shown in the same (arbitrary) units. (*Bottom frame*) The FL profiles for the same realizations as in top frame (and in the same units), but calculated without taking into account the relaxation-induced broadening. Note that the reddest FL profile in this case has the opposite asymmetry and the peak position shifted from 890 to 873 nm.

*middle frames*). To visualize the shapes of the exciton wavepacket (given by a superposition of the exciton wavefunctions) we calculate the density matrix in the site representation, i.e., $\rho_{nm} = \sum_{kk'} \rho_{kk'} c_n^k c_m^{k'}$. In the steady-state limit (after exciton relaxation) $\rho_{kk'} = \delta_{kk'} P_k$, where $P_k$ is the Boltzmann distribution of the exciton populations. In Fig. 6 (*right frames*) we show the steady-state density matrices at room temperature for the chosen realizations. The distribution in the diagonal direction, i.e., $\rho_{nn}$ shows the area of a noncoherent delocalization of the excitation. The width of the density matrix in the antidiagonal direction gives the coherence length of the exciton (which is always less than the width of the distribution in the diagonal direction).

The first, most delocalized exciton is characterized by relatively small shifts of the site energies, which are all less than the interpigment interaction energy ($M$ = 270–290 $cm^{-1}$). Moreover these shifts have a partially correlated character, i.e., the pigments $n$ = 5–9 are almost uniformly blue-shifted by 100–150 $cm^{-1}$, pigments $n$ = 10–14 × 30–100 $cm^{-1}$, etc., so that in most cases the relative shift between neighboring pigments is much less than the interaction between them. This amount of disorder does not destroy significantly the unperturbed (delocalized) states. Thus, the lowest exciton state is delocalized over the whole ring, but due to disorder the distribution of the wavefunction amplitudes is not uniform (as it must be in the homogeneous limit). Although each of the individual wavefunctions is delocalized, their superposition at room temperature results in a more localized wavepacket. The density matrix displays a coherence length (FWHM in the antidiagonal direction) of ~5–6 molecules due to thermal mixing of the states. The distribution along the diagonal direction shows no preferred localization site on the ring. So, for the dynamics we can expect the motion of a wavepacket delocalized over 5–6 pigments around the whole ring (as we will show below).

In case of the second realization of static disorder (intermediate FL peak) the site energy shifts are not significantly larger, but they are less correlated. For example, there is a number of neighboring pigments (like $n$ = 4–5, 6–7, 9–10, and 11–12 in this example) with opposite signs of the shift. The difference in energies starts to exceed the coupling $M$ between these sites. For these intermediate realizations the lowest exciton state becomes more localized. The corresponding wavefunction has a pronounced maximum at the red-most pigment, $n$ = 10. In the steady-state limit the wavepacket (with a coherence length of ~3–4 molecules) is localized near the sites $n$ = 10 or $n$ = 4.

The third realization (red FL peak) is similar to the second one, but with larger and uncorrelated site shifts that exceed significantly the $M$ value. The $k$ = 0 wavefunction is localized with a main peak at $n$ = 2 and a smaller one at $n$ = 4. The wavepacket is localized near $n$ = 2 with some small coherence between the $n$ = 2 and $n$ = 4 sites.

The forth realization demonstrates yet another scenario of localization. In this case the major part of the pigments exhibits a correlated shift (as in the first realization), but one pigment ($n$ = 4) has a very large red shift. This determines the almost complete localization of the $k$ = 0 state on the $n$ = 4 site and localization of the wavepacket on that same site without sizable coherence with other sites.

## Coherent dynamics of the density matrix

The diagonal elements of the steady-state density matrix $\rho_{nn}$ (Fig. 6) display the probability of population of the n-th site of the B850 ring. The population distribution is different for different realizations of the disorder. Thus, a small amount of disorder is characterized by a more or less uniform distribution, i.e., the excitation (coherently delocalized over a few molecules) can be found on any part of the ring. On the other hand, a larger amount of disorder leads to predominant

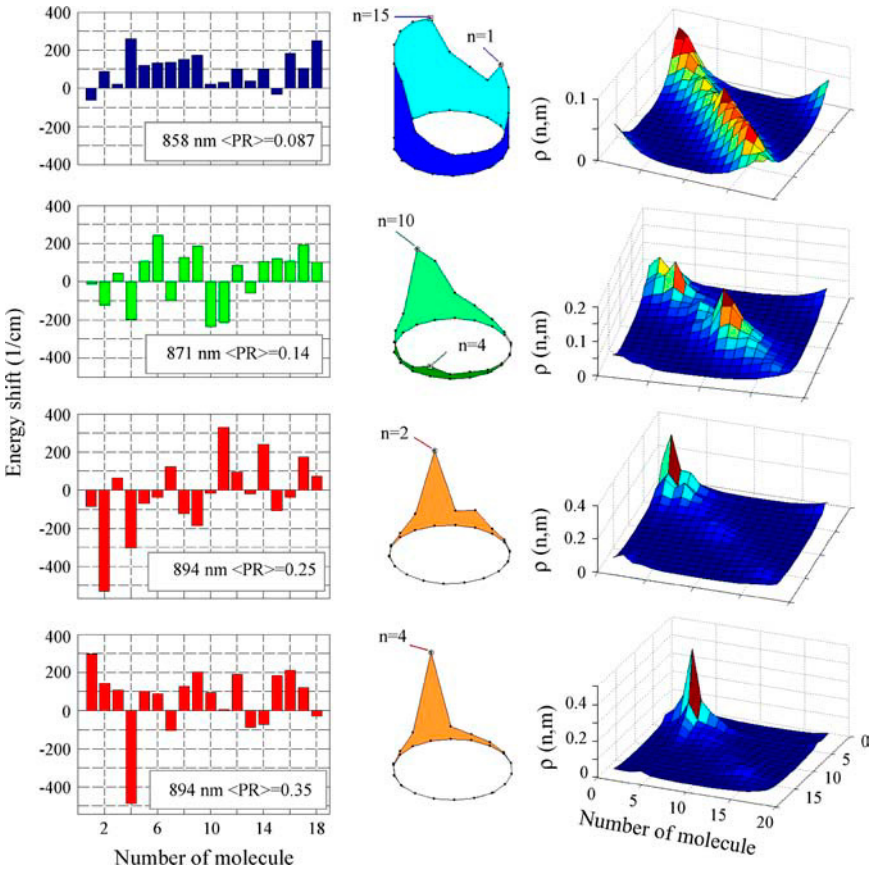


FIGURE 6 Site energies, exciton wavefunctions, and density matrices for the four different realizations of the disorder with the FL peaking at 858, 871, 894, and 894 nm and $\langle PR \rangle$ values of 0.087, 0.14, 0.25, and 0.35, respectively. (*Left column*) The shifts of the transition energies (from the unperturbed values) of the sites from $n = 1$ to $n = 18$. (*Middle column*) Participation of the n-th site in the lowest exciton state, given by the squared wavefunction amplitude $(c_n^k)^2$ for $k = 0$. The circle in the horizontal plane corresponds to the plane of the B850 ring, the points mark the positions of the sites from $n = 1$ to $n = 18$. For each case the site corresponding to maxima of the wavefunctions is indicated. Numbering of the sites is clockwise. (*Right column*) Steady-state density matrix in the site representation $\rho(n,m)$ at room temperature.

localization of the excitation on a group of pigments, or even on a single site.

We wish to study the dynamics of the excitation for these limiting cases. To this end we calculate the time evolution of the density matrix for the same realizations as in Fig. 6. We restrict to coherent dynamics, i.e., we calculate the motion of the initially prepared wavepacket without taking into account the relaxation of the one-exciton populations and the decay of coherences between one-exciton states. The coherent dynamics in the eigenstate basis is calculated using the Liouville equation for $\rho_{kk'}(t)$ (without including a relaxation tensor), with the initial conditions corresponding to the coherent wavepacket $\rho_{kk'}(t = 0) = (P_k\ P_{k'})^{1/2} \exp(i\phi_k - i\phi_{k'})$, with the steady-state populations $\rho_{kk}(t = 0) = P_k$ and arbitrarily fixed phases $\phi_k$ of the exciton states (in principle such a wavepacket could be created using a specially shaped laser pulse). The time evolution of the density matrix in the site representation is $\rho_{nm}(t) = \sum_{kk'} \rho_{kk'}(t) c_n^k c_m^{k'}$. Notice that the initial phases determine the location of the wavepacket within the ring at $t = 0$, but do not influence the character of its time evolution. The time evolution of the site populations $\rho_{nn}(t)$ during the 0–1.1-ps and 0–200-fs time intervals is shown in Figs. 7 and 8, respectively.

For the first realization with insignificant disorder the wavepacket delocalized over 4–6 molecules moves in a wavelike fashion around the ring. The initially created wavepacket has its maximum population amplitude at sites $n = 15$–$16$ (see Fig. 9) with an additional smaller maximum at $n = 2$. The full passage of the main maximum around the whole ring occurs in 200 fs. Note that a second maximum moves in the opposite direction (this dynamics is clearly seen during the first 100 fs, when the two maxima move toward each other). At 100 fs they meet, and after that the motion of the smaller maximum is hardly distinguishable. If we look at the dynamics on the 1-ps timescale it becomes clear that the wavelike motion is more pronounced during the first 200 fs (Fig. 7). For larger delays the coherent dynamics looks more like the interference of the waves destroyed by their scattering on impurities. First of all it should be noticed that the dynamics of the coherences $\rho_{kk'}(t) = \rho_{kk'}(0)\exp(i\omega_k t - i\omega_{k'} t)$, induces increasingly large dephasing at large delays. Due to this additional maxima can appear at larger delays instead of a single main maximum at $t = 0$. Secondly, even without such a dephasing, the distribution of the site populations $\rho_{nn}(t)$ may have a complicated form (with a lot of maxima) due to the disorder that destroys the shape of the exciton wavefunctions. As a result we obtain a complex time-dependent redistribution of the excitation density between many maxima instead of a perfect aberration-free motion of a single wave. But some wavelike features are still clearly distinguishable even at larger delays. Some maxima

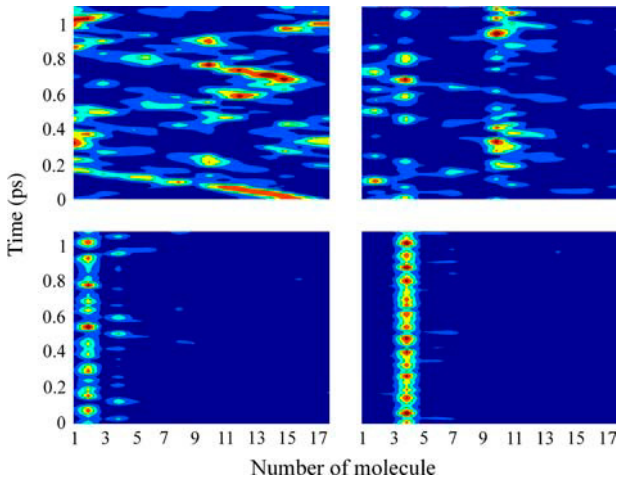


FIGURE 7 Coherent dynamics of the density matrix, i.e., calculated without relaxation of populations and coherences. Initial ($t = 0$) populations correspond to a thermally equilibrated wavepacket at room temperature, initial coherences have arbitrary fixed phases. Diagonal elements of the density matrix in the site representation $\rho(n,n)$ are shown as a function of time for the same realizations as in Fig. 6, i.e., for realizations with the $\langle PR \rangle$ values of 0.087 (*left top*), 0.14 (*right top*), 0.25 (*left bottom*), and 0.35 (*right bottom*).

exhibit a well-pronounced motion around the ring (in both directions) with the same time constant (~100 fs to pass over half of the ring).

For the second realization the excitation is delocalized over the sites $n = 2$–4 or $n = 10$–13. The calculated dynamics strongly resembles the hopping of the excitation from one group to the other with a time constant of ~350 fs. Thus, between 0 and 150 fs the excitation is on the $n = 2$–4 group, then from 150 to 500 fs the sites $n = 10$–13 are populated, between 500 and 850 fs the excitation is again on the $n = 2$–4 group. Within the $n = 2$–4 group there are oscillations between the sites $n = 2$ and $n = 4$ with a time constant of ~50 fs (corresponding to a jump from $n = 2$ to $n = 4$ or vise versa). Similar oscillations occur between the site $n = 10$ and sites $n = 11$–13. The wavelike motion observed for the first realization with small disorder is almost absent in this case, but it is possible to recognize some wavelike flow of excitation density from one group to another through the intermediate site $n = 7$. Due to the much stronger disorder the wavelike motion is destroyed by scattering on impurities, producing a lot of secondary waves moving in both directions. This results in a complicated nonuniform standing-wave pattern with oscillating populations of some sites (whereas other sites are almost not populated). Generally for a disordered system we always get a superposition of propagating waves and standing waves. For example, in the first realization besides the pronounced wavelike motion one can see some oscillations between the $n = 10$–16 and $n = 17$–18, 1–3 group with the time constant (half of period) of 350 fs.

In an ensemble experiment the combination of the wavelike motion and the hopping-type dynamics with time constants of 100 and 350 fs should give rise to similar components in the anisotropy decay kinetics. This prediction is in surprisingly good agreement with the observed biexponential polarization decay with 100 and 400 fs components in fluorescence upconversion experiments for LH1 (40) and the B850 ring of LH2 (41).

In the third realization of static disorder the excitation stays on the $n = 2$ site with some hopping to the $n = 4$ site. But the average population of the $n = 4$ site remains relatively small.

For the fourth realization the excitation is completely localized at one site, i.e., $n = 4$ without any migration to the other sites. But there is still some oscillatory modulation of the $n = 4$ population due to small coherences between the $n = 4$ and neighboring sites.

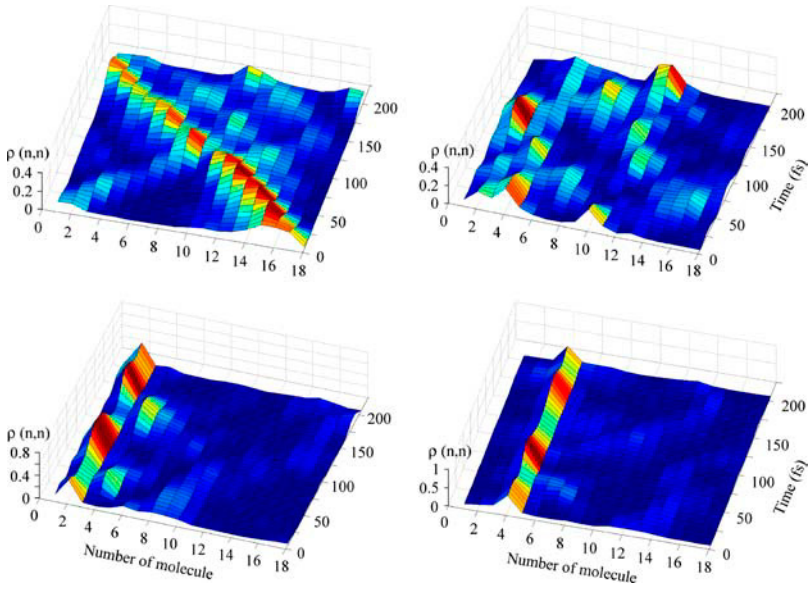


FIGURE 8 The same as in Fig. 7, but for a timescale of 0–200 fs.

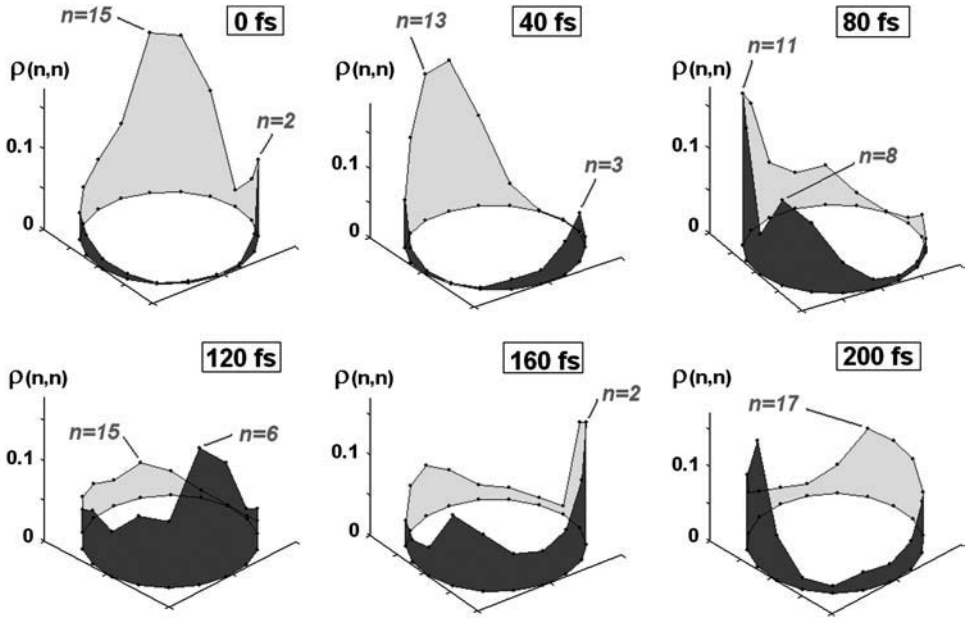


FIGURE 9 The shapes of the exciton wavepacket (distribution of diagonal elements of the density matrix $\rho(n,n)$ over $N$ sites of the ring) at fixed delays for the 858-nm realization shown in Figs. 6–8.

All of these excitation dynamics scenarios are associated with specific realizations of the static disorder. Thus, in a single-molecule experiment we observe realizations corresponding to physically different limits of the excitation dynamics, i.e., coherent wavelike motion of a delocalized exciton (with a 100-fs pass over half of the ring), hopping-type motion of the wavepacket (with 350-fs jumps between separated groups of 3–4 molecules), and self-trapping of an excitation that does not move from its localization site (Figs. 7–9).

## Circular and elliptical antenna models

In our model we assume random Gaussian static energetic disorder. Alternatively, a partially correlated disorder due to elliptical structural deformation has been proposed to interpret the low-temperature polarized fluorescence measurements (12,37,42). In the following we compare the exciton structure of the 850-nm band for these two possibilities.

In a homogeneous ring only the doubly degenerate $k = \pm 1$ exciton level is allowed, whereas the lowest $k = 0$ and other levels are forbidden by the symmetry of the ring. Introducing the disorder induces a splitting between the $k = \pm 1$ levels in proportion to $\sigma/M$, where $\sigma$ is the FWHM of the Gaussian distribution of uncorrelated disorder of pigment site energies, and $M$ is the pigment-pigment interaction energy (33). The disorder value required to explain a broad absorption of the B850 band in the LH2 and LH1 is ~400–500 $cm^{-1}$ (4–9,33,34). This is associated with a splitting between the $k = \pm 1$ levels of 70–80 $cm^{-1}$. Additionally, these levels borrow significant part of their dipole strength to the nearest exciton states. In particular, the lowest $k = 0$ level becomes strongly allowed (even superradiant). It is remarkable that the experimental superradiance value (2.8 for LH2 (43)) is very close to that predicted by the disordered model with $\sigma = 420$–$450$ $cm^{-1}$ (8,34).

Alternatively, the low-temperature single-molecule polarized fluorescence studies gave the splitting between the $k = \pm 1$ levels of 110 $cm^{-1}$ (13), which is difficult to explain with the disordered model. Naturally, such a splitting could be interpreted by further increasing the disorder, but in the case of uncorrelated disorder this will broaden the spectrum due to the increase of the dipole strength and the splitting between the other levels. In principle, a splitting between the $k = \pm 1$ levels without significant influence on the other levels is possible with any type of spectral or structural disorder correlated with the shape of the $k = -1$ and $k = 1$ wavefunctions. The latter have a form of $\cos(2\pi n/N)$ and $\sin(2\pi n/N)$ in the homogeneous limit, reaching their maximal amplitudes at the opposite sides of the ring in the $x$ and $y$ directions, respectively. Thus, any perturbation proportional to $\sin(4\pi n/N)$ has different signs near the $k = -1$ and $k = 1$ maximums, shifting these levels in opposite directions. Such a perturbation can be created by a correlated shift of the site energies in an unperturbed ring or a modulation of the coupling strength (and/or site energies) associated with an elliptical deformation (12,37,42). Due to a smaller distortion of the exciton states (compared to the random disordered model) this model predicts larger exciton delocalization and only weakly allowed $k = 0$ exciton level (12,13,42). The latter, however, is in contradiction with the experimentally observable superradiance of the $k = 0$ (43).

## Disordered ring versus elliptical deformations: modeling of single-molecule spectral profiles

In the following we investigate how the room-temperature fluorescence spectral profile shapes with different peak

wavelengths calculated with the two models of energetic disorder compare with our experimental results.

As we have seen (Fig. 2) the disordered model requires relatively large uncorrelated disorder values to obtain the splitting between the main exciton components necessary to simulate the absorption spectrum. In our model with the uncorrelated disorder value of $\sigma = 370$ cm$^{-1}$ the splitting between the $k = \pm 1$ energy levels is 40, 65, and 100 cm$^{-1}$ for realizations with the FL peak at 860, 870, and 890 nm, respectively (Fig. 2). The important feature is the increasingly bigger splitting between the $k = \pm 1$ levels and the intense $k = 0$ transition for more disordered realizations producing the specific shape of the red-shifted FL spectra.

To study the effect of ellipticity we restrict ourselves to the case of the deformation-induced modulation of the site energies $\Delta E_n$ in combination of the reduced amount of random (uncorrelated) disorder of the site energies $\sigma$. We suppose that $\Delta E_n = \Delta E \sin(4\pi(n - n_0)/N)$, where $\Delta E$ is taken from a Gaussian distribution with the FWHM of $\sigma_{corr}$ and with $\langle \Delta E \rangle = 0$. Generally the first moment $\langle \Delta E \rangle$ can be nonzero, but this does not change significantly the results discussed below. Because we do not consider the polarization of the emission, the $n_0$ value (that determines the principle axes of ellipses) is taken arbitrary. Generally, both the $n_0$ and $\Delta E$ values are fluctuating according to experimental observations (10). With such a model the bulk absorption and averaged FL spectra can be explained by taking $\sigma_{corr} = 275$ cm$^{-1}$ and $\sigma = 125$ cm$^{-1}$ (instead of $\sigma_{corr} = 0$ and $\sigma = 370$ cm$^{-1}$ in the disordered model). The averaged $k = \pm 1$ splitting is now increased up to 120 cm$^{-1}$. The emission profiles calculated for occurrences with different FL peak positions are shown in Fig. 10.

Comparison of the disordered (Fig. 2) and elliptical model (Fig. 10) shows that in the latter case we have a larger $k = \pm 1$ splitting (due to ellipticity), but lower intensities of the lowest $k = 0$ level (due to lower values of uncorrelated disorder). Moreover, the disorder-induced red shift of the $k = 0$ transition (responsible for the broadened and specifically shaped red-shifted FL profiles in the disordered model) is absent in the elliptical model with the reduced disorder value.

In the elliptical model the blue-shifted (860 nm) emission originates from the B850 ring weakly perturbed both by random and correlated shifts of the site energies. In this case the $k = \pm 1$ levels are almost degenerated and contribute equally to the emission (Fig. 10, *top*).

Realizations with a bigger elliptical deformation produce an increased splitting between the $k = \pm 1$ levels, so that the emission is determined mostly by the lower, $k = -1$ state giving FL profiles peaking at 870 nm (Fig. 10, *middle*). Due to the anomalously big $k = \pm 1$ splitting the $k = 1$ level is only weakly populated, whereas the lowest $k = 0$ state is almost forbidden. Thus, the contribution of the $k = 1$ and $k = 0$ states to the emission is much lower (as compared with the disordered model), thus producing narrower FL profiles at 870 nm.

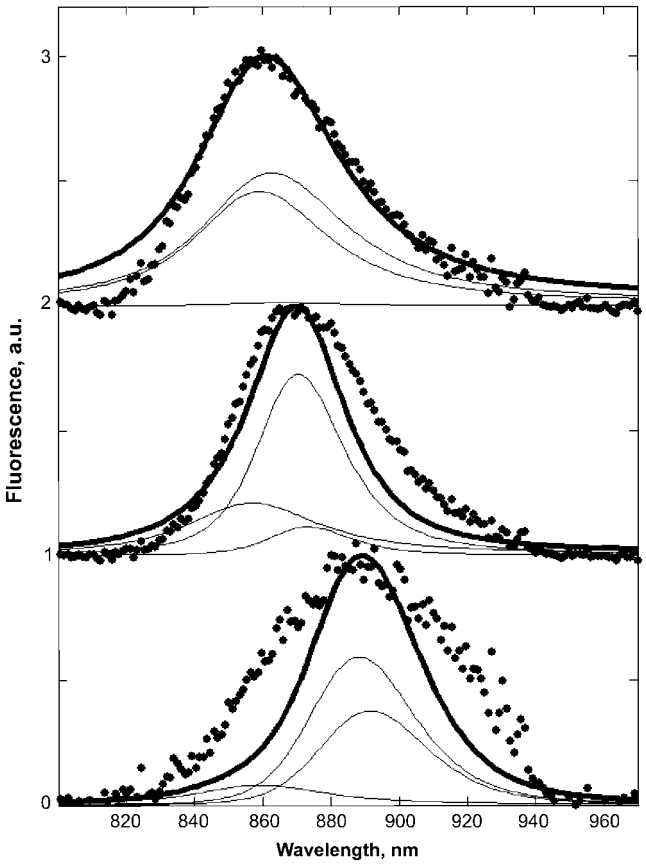


FIGURE 10 The same as in Fig. 2, but for the model with elliptical deformation. The values of the correlated and random (uncorrelated) disorder of the site energies are 275 and 125 cm$^{-1}$, respectively.

The $k = 0$ level becomes more intense for the red-shifted realizations, but its relative contribution is still not so much pronounced as in the disordered model (as well as its shift from the $k = -1$ level is not as large). Thus, the FL spectra peaking at 890 nm are determined mostly by the $k = -1$ level with some contribution of the almost nonshifted $k = 0$ level. Such a configuration of the exciton levels makes it impossible to reproduce the broad experimental FL profile (Fig. 10, *bottom*).

We conclude that the exciton structure predicted by the elliptical model considered here (which is in fact typical for all the models with elliptical deformations) is not consistent with the observed changes in FL spectra.

## Comparison of different experimental approaches

From the previous sections it appears that the interpretation of the different experimental data requires assuming different disorder models. In the following we seek the possible explanation of this apparent discrepancy in the variation of the sample preparation and measurement procedure.

In the room-temperature experiment by Bopp et al. FL spectra peak position exhibits a distribution with a FWHM of $\sim$100 cm$^{-1}$ (see Fig. 8 in Bopp et al. (10)), which is similar

to our measurements (see *histogram* in Fig. 1). The width of the FL spectrum fluctuates by $>200\ cm^{-1}$ (10) again in agreement with our data. However, the authors do not investigate if the elliptical deformation is required to explain the observed FL spectral line shapes. At the same time the ellipticity hypothesis in the low-temperature studies (11–13) is based solely on the polarization of the fluorescence-excitation spectra, whereas the shapes of the FL spectra were not studied. On the other hand, our measurements were indiscriminate for the spectral polarization. Thus, the direct comparison of the two types of measurements cannot be made at the moment.

It is possible that the difference in the model assumptions required to interpret the different experimental data originates from the sample preparation conditions. In our ambient temperature experiment complexes are immobilized on a ''carpet'' of amino groups of poly-l-lysine and submerged in a physiological buffer and thus are in a radically different environment than in the case where they are spin-coated in a PVA matrix at cryo-temperature as in van Oijen et al. (13).

## CONCLUSIONS

We show that the model of the disordered ring allows a quantitative interpretation of the single-molecule spectroscopic data for LH2. The positions and spectral shapes of the main exciton components of the B850 ring are determined in this model by the disorder-induced shift of the exciton eigenvalues in combination with phonon-induced effects (i.e., reorganization shift and broadening, that increase in proportion to the inverse delocalization length of the exciton state). Being dependent on the realization of the disorder, these factors produce different forms of the emission profile. In addition, different delocalization degrees and effective couplings to phonons determine different types of the excitation dynamics in these realizations. We demonstrate that experimentally observed quasistable conformational states are characterized by the excitation energy transfer regimes varying from a coherent wavelike motion of a delocalized exciton to a hopping-type motion of a wavepacket (with jumps between separated groups of 3–4 molecules) and self-trapping of a localized excitation.

The alternative models that assume elliptical deformations of the ring fail to explain the spectral shapes of the experimentally observed emission profiles corresponding to different FL peak positions.

This research was supported by the Netherlands Organization for Scientific Research (NWO). V.N. was supported by the Dutch (NWO)-Russian scientific cooperation program, grant No. 047.016.006.

## REFERENCES

1. van Grondelle, R., J. P. Dekker, T. Gillbro, and V. Sundström. 1994. Energy-transfer and trapping in photosynthesis. *Biochim. Biophys. Acta*. 1187:1–65.
2. McDermott, G., S. M. Prince, A. A. Freer, A. M. Hawthornthwaite, M. Z. Papiz, R. J. Cogdell, and N. W. Isaacs. 1995. Crystal structure of an integral membrane light-harvesting complex from photosynthetic bacteria. *Nature*. 374:517–521.
3. Papiz, M. Z., S. M. Prince, T. Howard, R. J. Cogdell, and N. W. Isaacs. 2003. The structure and thermal motion of the B800–850 LH2 complex from *Rps. acidophila* at 2.0 Å resolution and 100 K: new structural features and functionally relevant motions. *J. Mol. Biol*. 326:1523–1538.
4. Sundström, V., T. Pullerits, and R. van Grondelle. 1999. Photosynthetic light-harvesting: reconciling dynamics and structure of purple bacterial LH2 reveals function of photosynthetic unit. *J. Phys. Chem. B*. 103:2327–2346.
5. van Grondelle, R., and V. Novoderezhkin. 2001. Dynamics of excitation energy transfer in the LH1 and LH2 light-harvesting complexes of photosynthetic bacteria. *Biochemistry*. 40:15057–15068.
6. Hu, X. C., T. Ritz, A. Damjanovic, F. Autenrieth, and K. Schulten. 2002. Photosynthetic apparatus of purple bacteria. *Q. Rev. Biophys*. 35:1–62.
7. Meier, T., V. Chernyak, and S. Mukamel. 1997. Multiple exciton coherence sizes in photosynthetic antenna complexes viewed by pump-probe spectroscopy. *J. Phys. Chem. B*. 101:7332–7342.
8. Novoderezhkin, V., R. Monshouwer, and R. van Grondelle. 1999. Exciton (de)localization in the LH2 antenna of *Rhodobacter sphaeroides* as revealed by relative difference absorption measurements of the LH2 antenna and the B820 subunit. *J. Phys. Chem. B*. 103:10540–10548.
9. Dahlbom, M., T. Pullerits, S. Mukamel, and V. Sundström. 2001. Exciton delocalization in the B850 light-harvesting complex: comparison of different measures. *J. Phys. Chem. B*. 105:5515–5524.
10. Bopp, M. A., A. Sytnik, T. D. Howard, R. J. Cogdell, and R. M. Hochstrasser. 1999. The dynamics of structural deformations of immobilized single light-harvesting complexes. *Proc. Natl. Acad. Sci. USA*. 96:11271–11276.
11. Ketelaars, M., A. M. van Oijen, M. Matsushita, J. Köhler, J. Schmidt, and T. J. Aartsma. 2001. Spectroscopy on the B850 band of individual light-harvesting 2 complexes of *Rhodopseudomonas acidophila*. I. Experiments and Monte Carlo simulations. *Biophys. J*. 80:1591–1603.
12. Matsushita, M., M. Ketelaars, A. M. van Oijen, J. Köhler, T. J. Aartsma, and J. Schmidt. 2001. Spectroscopy on the B850 band of individual light-harvesting 2 complexes of *Rhodopseudomonas acidophila*. II. Exciton states of an elliptically deformed ring aggregate. *Biophys. J*. 80:1604–1614.
13. van Oijen, A. M., M. Ketelaars, J. Köhler, T. J. Aartsma, and J. Schmidt. 1999. Unraveling the electronic structure of individual photosynthetic pigment-protein complexes. *Science*. 285:400–402.
14. Hofmann, C., T. J. Aartsma, H. Michel, and J. Köhler. 2003. Direct observation of tiers in the energy landscape of a chromoprotein: a single-molecule study. *Proc. Natl. Acad. Sci. USA*. 100:15534–15538.
15. Scheuring, S., F. Reiss-Husson, A. Engel, J. L. Rigaud, and J. L. Ranck. 2001. High-resolution AFM topographs of *Rubrivivax gelatinosus* light-harvesting complex LH2. *EMBO J*. 20:3029–3035.
16. Rutkauskas, D., V. Novoderezhkin, R. J. Cogdell, and R. van Grondelle. 2005. Fluorescence spectroscopy of conformational changes of single LH2 complexes. *Biophys. J*. 88:422–435.
17. Rutkauskas, D., V. Novoderezkhin, R. J. Cogdell, and R. van Grondelle. 2004. Fluorescence spectral fluctuations of single LH2 complexes from *Rhodopseudomonas acidophila* strain 10050. *Biochemistry*. 43:4431–4438.
18. Mukamel, S. 1995. Principles of Nonlinear Optical Spectroscopy. Oxford University Press, New York.
19. Zhang, W. M., T. Meier, V. Chernyak, and S. Mukamel. 1998. Exciton-migration and three-pulse femtosecond optical spectroscopies of photosynthetic antenna complexes. *J. Chem. Phys*. 108:7763–7774.
20. Ohta, K., M. Yang, and G. R. Fleming. 2001. Ultrafast exciton dynamics of J-aggregates in room temperature solution studied by

third-order nonlinear optical spectroscopy and numerical simulation based on exciton theory. *J. Chem. Phys.* 115:7609–7621.

21. Wendling, M., M. A. Przyjalgowski, D. Gullen, S. I. E. Vulto, T. J. Aartsma, R. van Grondelle, and H. van Amerongen. 2002. The quantitative relationship between structure and polarized spectroscopy in the FMO complex of *Prosthecochloris aestuarii*: refining experiments and simulations. *Photosynth. Res.* 71:99–123.
22. Renger, T., and R. A. Marcus. 2002. Photophysical properties of PS-2 reaction centers and a discrepancy in exciton relaxation times. *J. Phys. Chem. B.* 106:1809–1819.
23. Raszewski, G., W. Saenger, and T. Renger. 2005. Theory of optical spectra of photosystem II reaction centers: location of the triplet state and the identity of the primary electron donor. *Biophys. J.* 88:986–998.
24. Novoderezhkin, V. I., E. G. Andrizhiyevskaya, J. P. Dekker, and R. van Grondelle. 2005. Pathways and timescales of primary charge separation in the photosystem II reaction center as revealed by a simultaneous fit of time-resolved fluorescence and transient absorption. *Biophys. J.* 89:1464–1481.
25. Novoderezhkin, V. I., M. A. Palacios, H. van Amerongen, and R. van Grondelle. 2004. Energy-transfer dynamics in the LHCII complex of higher plants: modified Redfield approach. *J. Phys. Chem. B.* 108: 10363–10375.
26. Novoderezhkin, V. I., M. A. Palacios, H. van Amerongen, and R. van Grondelle. 2005. Excitation dynamics in the LHCII complex of higher plants: modeling based on the 2.72 Å crystal structure. *J. Phys. Chem. B.* 109:10493–10504.
27. Yang, M., and G. R. Fleming. 2002. Influence of phonons on exciton transfer dynamics: comparison of the Redfield, Förster, and modified Redfield equations. *Chem. Phys.* 275:355–372.
28. Peterman, E. J. G., T. Pullerits, R. van Grondelle, and H. van Amerongen. 1997. Electron-phonon coupling and vibronic fine structure of light-harvesting complex II of green plants: temperature dependent absorption and high-resolution fluorescence spectroscopy. *J. Phys. Chem. B.* 101:4448–4457.
29. Pieper, J., J. Voigt, and G. J. Small. 1999. Chlorophyll a Franck-Condon factors and excitation energy transfer. *J. Phys. Chem. B.* 103: 2319–2322.
30. Damjanovic, A., I. Kosztin, U. Kleinekathoefer, and K. Schulten. 2002. Excitons in a photosynthetic light-harvesting system: a combined molecular dynamics, quantum chemistry, and polaron model study. *Phys. Rev.* 65:031919.
31. Fidder, H., J. Knoester, and D. A. Wiersma. 1991. Optical properties of disordered molecular aggregates: a numerical study. *J. Chem. Phys.* 95:7880–7890.
32. Meier, T., Y. Zhao, V. Chernyak, and S. Mukamel. 1997. Polarons, localization, and excitonic coherence in superradiance of biological antenna complexes. *J. Chem. Phys.* 107:3876–3893.
33. Novoderezhkin, V., R. Monshouwer, and R. van Grondelle. 1999. Disordered exciton model for the core light-harvesting antenna of *Rhodopseudomonas viridis*. *Biophys. J.* 77:666–681.
34. Novoderezhkin, V., M. Wendling, and R. van Grondelle. 2003. Intra- and interband transfers in the B800–B850 antenna of *Rhodospirillum molischianum*: Redfield theory modeling of polarized pump-probe kinetics. *J. Phys. Chem. B.* 107:11534–11548.
35. Jung, Y., E. Barkai, and R. J. Silbey. 2002. Current status of single-molecule spectroscopy: theoretical aspects. *J. Chem. Phys.* 117:10980–10995.
36. Dempster, S. E., S. J. Jang, and R. J. Silbey. 2001. Single molecule spectroscopy of disordered circular aggregates: a perturbation analysis. *J. Chem. Phys.* 114:10015–10023.
37. Jang, S., and R. J. Silbey. 2003. Single complex line shapes of the B850 band of LH2. *J. Chem. Phys.* 118:9324–9336.
38. Sauer, K., R. J. Cogdell, S. M. Prince, A. Freer, N. W. Isaacs, and H. Scheer. 1996. Structure-based calculations of the optical spectra of the LH2 bacteriochlorophyll-protein complex from *Rhodopseudomonas acidophila*. *Photochem. Photobiol.* 64:564–576.
39. Alden, R. G., E. Johnson, V. Nagarajan, W. W. Parson, C. J. Law, and R. J. Cogdell. 1997. Calculations of spectroscopic properties of the LH2 bacteriochlorophyll-protein antenna complex from *Rhodopseudomonas acidophila*. *J. Phys. Chem. B.* 101:4667–4680.
40. Bradforth, S. E., R. Jimenez, F. van Mourik, R. van Grondelle, and G. R. Fleming. 1995. Excitation transfer in the core light-harvesting complex (LH1) of *Rhodobacter sphaeroides*: an ultrafast fluorescence depolarization and annihilation study. *J. Phys. Chem.* 99:16179–16191.
41. Jimenez, R., S. N. Dikshit, S. E. Bradforth, and G. R. Fleming. 1996. Electronic excitation transfer in the LH2 complex of *Rhodobacter sphaeroides*. *J. Phys. Chem.* 100:6825–6834.
42. Mostovoy, M. V., and J. Knoester. 2000. Statistics of optical spectra from single-ring aggregates and its application to LH2. *J. Phys. Chem. B.* 104:12355–12364.
43. Monshouwer, R., M. Abrahamsson, F. van Mourik, and R. van Grondelle. 1997. Superradiance and exciton delocalization in bacterial photosynthetic light-harvesting systems. *J. Phys. Chem. B.* 101:7241–7248.